ISSN 2633-4828

International Journal of Applied Engineering and Technology

A new hole-down-array design for airfoil separation control

A. Teimourian, Didac Romero, and S. Altmeyer*
Castelldefels School of Telecom and Aerospace Engineering, Universitat Politècnica de Catalunya, 08034 Barcelona, Spain
(Dated: July 24, 2025)

***Abstract* - This study explores the feasibility of passive flow control utilizing a hole-down array (HDA), inspired by the natural observation of gaps in bird feathers during flight. We combine numerical simulations with experimental wind tunnel tests to assess the impact of HDA on the standard NACA0012 airfoil. We test two distinct HDA configurations: one featuring a single row of holes and the other with two rows, with the holes positioned either centrally along the airfoil or near the trailing edge. The aim is to evaluate these design alternatives and their potential to enhance performance. The aerodynamic coefficients and pressure distributions are computed using computational fluid dynamics (CFD), then compared and verified with wind tunnel test data. The findings are promising, indicating that these configurations could significantly boost lift without affecting drag. Although results vary with the angle of attack, the maximum lift-to-drag ratio can be improved relative to the original NACA0012 model. Additionally, we highlight the limitations encountered when employing 2D simulations for complex geometries.**

Index Terms - Flow control, Flow separation, Canonical holes, CFD, Hole-down-array, Wind tunnel

I. INTRODUCTION

The aviation industry is experiencing a significant surge, and as it moves towards a cleaner, more sustainable future, manufacturers globally are compelled to enhance efficiency. The latest generation of aircraft features wings with improved lift-to-drag ratios, which not only reduce fuel usage for a more eco-friendly approach but also boost operational profitability. With high levels of interest, the array of techniques under exploration to increase wing efficiency is extensive and ever-expanding. Notably, the quest for efficiency extends well beyond the aviation sector. For example, airfoils are critical components of wind turbine blades, heavily influencing flow characteristics and aerodynamic performance, thus playing a vital role in optimizing energy efficiency. A key challenge is that airfoils can stall at high angles of attack, leading to flow separation, thereby diminishing aerodynamic performance and flow characteristics. Consequently, controlling the flow over wind turbine blades focuses on minimizing flow separation, delaying stall, and enhancing the lift-to-drag ratio. The primary objective is to shift the separation point on the airfoil towards the trailing edge, which could result in more streamlined flow over the upper surface, thus boosting efficiency.

The primary aim of this research is to introduce an innovative airfoil/wing design concept, utilizing arrays of holes within the wing, with the objective of managing airflow and enhancing efficiency. Traditional flow management methods are typically divided into two categories: passive control, which does not require external power, and active control, which does require some form of power input. Despite these differences, the unified aim of all these approaches is to manipulate the boundary layer to boost the aerodynamic performance of the lifting surface. Consequently, numerous flow management techniques have been devised and evaluated over time. The existing body of literature on this subject is extensive, hence, we will focus only on the most pertinent works related to this study, leaving those interested to consult the references in the cited paper for further exploration. One widely-used passive technique is the Trapped Vortex Cavity or Trapped Vortex Cell (TVC) [1, 2], which involves an airfoil with a cavity on the upper side. The concept involves anchoring a vortex within the cavity, thereby creating a significant recirculation zone to delay flow separation [3, 4].

The overall influence of the cavity on the flow surrounding the airfoil pertains to the creation of vortices that diminish flow separation downstream of the cavity [5]. A primary issue with this method is that, depending on external conditions, the vortex exhibits instability [6], making it challenging to maintain if control over the cav-

*Electronic address: sebastian.andreas.altmeyer@upc.edu; URL: http://www.sebastianaltmeyer.de

ity area is not applied. Other widely used passive techniques employ various types of vortex generators [7, 8] or backward-facing step airfoils [9]. Furthermore, alternative wing shapes and configurations have been explored, such as upper surface flaps [10] or sinusoidal aerofoils at the trailing edge [11].

Fluidic actuators, often known as jet actuators [12–16], are the most prevalent techniques in active flow control, engaging the boundary layer on the airfoil's surface. These actuators function through suction, blowing, or a combination of both. Additionally, there is a wide range of temporal jet behaviors, from steady [15, 16], to oscillating [17], and even pulsing modes [18]. An alternative strategy is presented in the study by Dai *et al.* [19], which explores a traveling wave structure near the airfoil's leading edge. This study demonstrated that by optimizing the length-width ratio for the traveling wave, improvements in aerodynamic performance can be achieved due to the postponement of flow separation.

The newly proposed HDA design presents another instance of a passive method, enabling the control of the boundary layer and, consequently, flow separation. To our knowledge, the studies by Xie *et al.* [20] and Paul *et al.* [21] are the only ones that share a concept similar to the newly proposed HDA design. They used a slot in the airfoil, known as a split blade, as a novel flow control mechanism. Their findings indicated that the separation area expands with an increase in the angle of attack while the separation point shifts upstream.

This study aims to explore the flow dynamics surrounding a new wing design, which is based on the NACA-0012 airfoil, by examining one or two hole down arrays (HDA-1 and HDA-2) located between the center and trailing edge. The fundamental motivation for our innovative HDA design is inspired by bird wings, which have evolved and optimized over time to be highly efficient for flight. This concept aims to induce multiple separation points [22–25]. We employ numerical simulations using the FLUENT-Ansys solver and Solidworks, alongside experimental measurements, to compare and validate our findings. Various angles of attack α and airspeeds are evaluated. Schematics of the airfoil and wing design, including conical holes, are depicted in Figs. 1 and 2. Further details on the airfoil design elements are provided in Sec. II A.

Nomenclature:

AoA	angle of attack
C_l	coefficient of lift
C_d	coefficient of drag
C_p	coefficient of pressure
L/D	lift to drag ratio
Re	Reynolds number
v	free stream velocity
ρ	air density
RANS	Reynold's Averaged Navier Stokes Equation
HDA	Hole down array
HDA-1	Hole down array design 1 - large holes near trailing edge
HDA-2	Hole down array design 2 - small holes near center and large holes near trailing edge

II. PROBLEM FORMULATION AND METHODOLOGY

This research assesses the impact of novel wing designs incorporating a hole down array (HDA). Starting with a standard NACA0012 airfoil (Fig. 1(a)), two innovative wing configurations were created and evaluated. We introduce two new models: the first features a *single row* of holes (HDA-1) (Fig. 1(b)), while the second incorporates *two rows* of holes (HDA-2) (Fig. 1(c)) with a staggered layout and varied hole sizes between rows. Various angles of attack α were tested, examining aerodynamic parameters such as lift coefficient c_l, drag coefficient c_d, lift-to-drag ratio c_L/c_D, and pressure distributions c_p. Numerical simulations were conducted alongside experimental wind tunnel tests to evaluate and compare outcomes. Initial conditions are detailed in Table I. Wind tunnel experiments were used to corroborate CFD results and enhance comprehension of fundamental fluid dynamics, especially concerning both two-dimensional (2D) and three-dimensional (3D) influences as well as potential turbulent transitions.

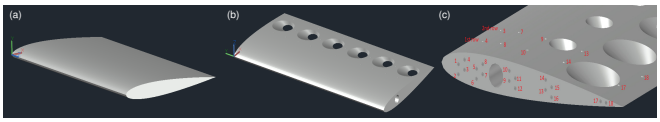

FIG. 1: Illustrations of (a) the base NACA0012 model, and the two new wing designs: (b) single row HDA-1 and (c) two row HDA-2. Numbers in (c) illustrate the hole numbers for pressure measurements (c_p) (Hierarchy of small holes for measuring pressure points first row (holes 4,8,10,14,17), second row (holes 3,7,9,13,18).

Figure 1 shows the drawings of the two novel designs for single row HDA-1 and two row HDA-2 configuration together with the corresponding baseline NACA0012 model. The dimensions were scaled down to fit the wind tunnel size and to guarantee a tunnel blockage factor of less than 5%. Accordingly, the scale-down factor was 6.25, which reduced the wing length (semi-span) to 30

cm and the chord at the root to 15 cm.

TABLE I: Initial conditions used in this study.

Parameter	value
Fluid	Air
density (ρ)	1.204 kg/m^3
Freestream Pressure	101325 Pa
Freestream temperature	288 K
Freestream velocity	22.63 m/s
kinematic viscosity	1.825×10^{-5} (kg/ms)
Re	10.56×10^5
Scheme	Variable
Turbulence model	Viscous SST $k-\omega$
α	$0° - 14°$

A. Design elements

Various works have shown that the largest pressure differences between the extradus and intradus (upper and lower surface) of an airfoil can be found around the separation point and thereafter that pressure differences decrease along the length of the chord line. Thus, the main lift is provided before about 60% of the chord line and only about 40% of the final part. Based on these observations, we propose that the holes be located after the midpoint of the chord line to support the generation of lift. As a baseline, we consider the NACA0012 symmetric (non-camber) airfoil. The four numbers in the NACA series indicate that the airfoil does not have any camber, and the number (12) indicates that the thickness of the airfoil is 12% of the chord length of the airfoil.

One key point is identifying the direction of the resulting flow stream within the HDA, particularly inside the holes. Based on the primary flight criterion, P2 is always greater than P1 (see Fig. 2(a)). Therefore, if the flow direction is upward, the velocity differential between the entry and exit points of the hole should be sufficient to overcome the pressure differential, according to Bernoulli's equation. On the other hand, if the flow direction is downward, this might accelerate the fluid inside the hole, indicating that a downward stream direction could be more efficient. According to the pressure distribution shown in Fig. 2, the pressures of the extradus and intradus do not fluctuate after the separation point. Consequently, altering the pressure distribution on the upper surface will cause the flow direction to shift from downward to upward. In contrast, changing the pressure distribution on the lower side will have the opposite effect, resulting in a flow direction that moves from the upper surface to the lower surface.

The dimensions and shape of the canonical holes significantly affect the results. In this study, we specifically consider dimensions that feature smaller cross-sectional areas on the lower surface and larger cross-sectional areas on the upper surface. For HDA-1 (see Fig. 2(a)), the parameters are $A1, r_1 = 2\,\text{cm}$ and $A2, r_2 = 1\,\text{cm}$. For HDA-2 (see Fig. 2(b)), there is a row close to the center with smaller holes, where $A1, r_1 = 1\,\text{cm}$ and $A2, r_2 = 0.5\,\text{cm}$, and a row near the trailing edge with larger holes, where $A1, r_1 = 2\,\text{cm}$ and $A2, r_2 = 1\,\text{cm}$.

The motivation behind these configurations and dimensions is that the higher pressure within the intradus will be released through the smaller area $A2$ into the hole, generating a vertical upward flow. However, due to the shape of the walls, it is hoped that this will not create an additional turbulent flow stream.

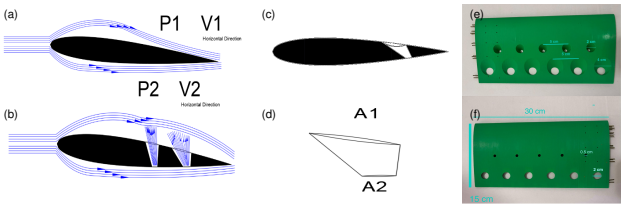

FIG. 2: Schematics of the canonical-hole design. (a) General shape of vortex around base airfoil NACA0012. (b) Combination vortex around airfoil with conical hole. (c, d) General shape of conical hole. (e, f) extradus and intradus of HDA-2 with indicated dimensions of the holes. The dimensions are: smaller holes $A1, r_1 = 1cm$, $A2, r_2 = 0.5cm$ and row close to the trailing edge with bigger holes $A1, r_1 = 2cm$, $A2, r_2 = 1cm$.

B. Methodology

To perform the numerical simulations we consider the Reynolds-averaged Navier-Stokes (RANS) equations (for more details see de Pieri [**?**]). In particular, we use the $k-\omega$ SST turbulence model, which is designed for low Reynolds number flows, and which excels in a high convergence rate and behavior when compared to other turbulent models.

1. *Mathematical model*

In general Computational fluid dynamics (CFD) is used to approximate physical problems into a mathematical model, most common a set of differential equations together with boundary conditions. The 3D continuity and Navier-Stokes equations, in general, can be written as follow

$$\begin{aligned} \nabla \cdot \mathbf{u} &= 0. \\ \rho(\partial_t + \mathbf{u} \cdot \nabla)\mathbf{u} &= -\nabla P + \mu \nabla^2 \mathbf{u} + \mathbf{F}, \end{aligned} \tag{2.1}$$

with the air density ρ, the velocity $\mathbf{v}$ (u, v, w) being the velocity compounds in the direction (x, y, z)), respectively. The pressure p, kinematic viscosity μ, and the external force $\mathbf{F}$ acting on the fluid.

3

2. Numerical simulations

In our study, the equations referenced in 2.1 are solved numerically using software tools such as ANSYS Fluent and SOLIDWORKS. The initial and boundary conditions are defined based on standard room temperature and pressure. The atmospheric far-field pressure, along with a specified Mach number, serves as the boundary for all far-field regions. We consider no-slip conditions on the wall surfaces, and the initial flow field condition is set in accordance with the free stream [26]. The geometry depicted in Fig. 3(b) is discretized using a 3D structured mesh with finite volumes for the Reynolds-Averaged Navier-Stokes (RANS) models. The dimensions of the computational domain are aligned with the inner dimensions of the wind tunnel: 0.75 m in the x-direction, 0.45 m in the y-direction, and 0.45 m in the z-direction. After meshing, the total number of nodes for each case was determined to be 345,670. This number was established by analyzing the discretization error relative to the element size; we considered a variation of both lift and drag coefficients within 2% as acceptable. The boundary conditions for the system were defined by treating the inner walls of the wind tunnel and the wing surfaces as solid with a no-slip condition. We tested different inlet velocities of air entering the wind tunnel (20, 25, and 30 m/s) with the outlet air condition set to atmospheric pressure, at 101325 Pa. A total of 1000 iterations was used as the stopping criterion, ensuring a balance between accuracy and the performance of the computer.

3. Computational Model

The theoretical framework of SOLIDWORKS Flow Simulation is founded on the integration of Computational Fluid Dynamics (CFD) directly within a Computer-Aided Design (CAD) environment. This approach leverages native CAD data for geometry representation, thereby streamlining the design-to-analysis workflow and ensuring high fidelity in simulation outcomes. By utilizing a CAD/CFD bridge, the system preserves detailed, high-quality three-dimensional product data throughout the product lifecycle, facilitating both virtual prototyping and accurate physical simulation.

Central to this framework is the use of Cartesian-based mesh generation. Here, an immersed-body meshing technique is employed to discretize the computational domain into a series of rectilinear, cuboidal cells that are classified as fully fluid, fully solid, or partial cells intersected by the solid-fluid interface. Partial cells are further subdivided into multiple control volumes to capture the intricacies of complex geometries, such as thin walls and intricate interface regions, thereby allowing accurate resolution even when using relatively coarse meshes. The mesh is adaptively refined based on geometric features such as curvature and small-scale details, ensuring that critical flow regions receive sufficient resolution.

Further the Two-Scale Wall Function (2SWF) approach for boundary layer treatment. This method addresses the challenges associated with resolving the high-gradient boundary layer near solid surfaces. When the mesh resolution is insufficient for direct resolution, an integrated thin boundary layer model based on the Prandtl approach is applied along fluid streamlines. In cases where the mesh is adequately refined, a thick boundary layer model employing the full near-wall velocity profile, as prescribed by Van Driest?s formulation, is used. In intermediate situations, a blended strategy ensures a smooth transition between these two regimes, thereby enabling accurate predictions of skin friction and heat flux.

In the simulation the full Navier-Stokes equations are solved for mass, momentum, and energy conservation, incorporating a modified $k?\epsilon$ turbulence model with damping functions to capture both laminar and turbulent flow regimes. The numerical methods employed include a pressure-velocity coupling strategy via a SIMPLE-like operator-splitting technique, combined with iterative solvers such as a preconditioned conjugate gradient method and a multigrid approach for efficient resolution of the pressure correction equation.

TABLE II: Mesh configuration

parameter	level	
	global	local
level of refining fluid cells	1	3
level of refining cells at fluid/solid boundary	2	4
maximum chanel refinement level	-	2
small solid feature refinement level	2	4
curvature level	2	5
tolerance level	2	3

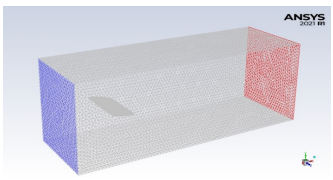

FIG. 3: Computational grid. Mesh distribution for airfoil (NACA0012) domain.

The convergence criteria selected for this problem is 10^{-5} for the scaled absolute residuals of continuity, 10^{-6} for the scaled absolute residuals of momentum equations and lastly 10^{-9} for the energy equation. For cases simulated with RANS, the convergence criterion for turbulent viscosity was 10^{-5}. Also, the convergence of airfoil's lift and drag at the stationary result is considered.

C. Experiments

Figure 4 illustrates the different printed wing designs: baseline NACA0012, HDA-1, and HDA-2. These wings were created using a 3D printer, which was modified to enhance the structural integrity of the models and ensure secure mounting (using an inserted steel rod) within the wind tunnel. Additionally, various small channels have been incorporated into the wing body to measure pressure at different locations across the surface of the wing.

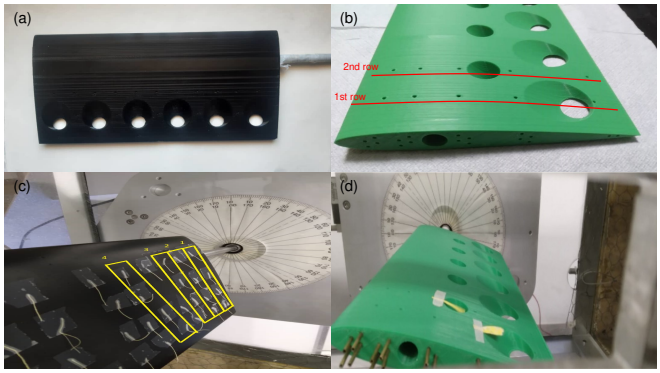

FIG. 4: Printed prototype for (a) single row HDA-1 and (b) two row HDA-2. Mounting of (c) the baseline NACA0012 3D model and the the new wing design HDA-2 in the wind tunnel. Red lines in (b) highlight cross section of the wing (airfoil) marked as 1st row and 2nd row with either large hole close to the tailing edge or smaller hole close to the center of the wing, respectively.

The two prototypes, HDA-1 and HDA-2, were printed using the highest possible resolution with stereo lithography (SLA) standard black/green resin. It is important to note that several sources of error can still affect accuracy, including components, calibration, materials, and post-curing processes. In this case, a high-resolution surface roughness was achieved with a layer thickness of 0.2 mm.

Considering that the maximum airspeed generated by the wind tunnel is 36.31 m/s and that the chord length of the prototype is 15 cm, the maximum Reynolds number Re achievable in the experiment is 6.15×10^5. For the experimental tests, we selected various velocities ranging from 20 to 30 m/s. For a valid comparison, we ensured that the same Reynolds numbers were used in the CFD simulations.

As an initial calibration, we used the baseline model (Fig. 1(a)) and conducted wind tunnel tests at different airspeeds of 20 m/s, 25 m/s, and 30 m/s. Starting at an angle of attack of $\alpha = 0°$ and increasing in increments of 2° until reaching the stall angle, we compared the experimental results of the measured aerodynamic forces with the values obtained from our simulations to validate the CFD results.

1. Experimental validation

a. Data uncertainty The wind tunnel equipment used is an open circuit with air stream input and output. It was calibrated at the manufacturing factory using the general NACA 0012 airfoil shape. Consequently, we decided to test the hole-drawn array design based on the basic shape of NACA 0012. Measurement precision data for all tests will be maintained at a confidence level of at least 95 percent.

In these tests, the angle of attack and velocity are the input data, while pressure, lift, and drag are the variable data to be measured. The speed is determined by frequency according to the following formula, with a correction coefficient of 0.9995 with $V = (0.733 f.s + 0.292)$ m/s. All measurements were taken after a 10-second relaxation time to ensure that any transient behaviors had dissipated. The uncertainty error is calculated using the formula:

$$U = \sqrt{B^2 + P^2}$$

where B is the bias error and P is the measurement precision error.

There are two independent methods for data extraction in this wind tunnel, with each method used to obtain variables separately. No data from one method is combined with another, ensuring that the bias limit of estimation is zero.

b. Metering pressure points To produce the pressure distribution graph, pressure points are located on both sides of the sampled airfoil. Each point is connected to the measurement system by a single tube. There is one exceptional point not located on the airfoil body, which is used to register the air stream pressure.

A total of 18 pressure points (see Table III) are distributed across the airfoil body for measuring static pressure, organized in two sets. The pressure coefficient graph can be calculated using the following formula:

$$C_P = \frac{P_i - P_{amb}}{0.5\rho V^2}$$

In this formula, P_i and P_{amb} represent the measured parameters during the test. To determine the precision error, we use the formula $\frac{1}{n^2}$, where $n = 18$, resulting in a precision error of $P = 0.31\%$. It is assumed that, for calculating bias error, the pressure coefficient has a linear relationship with the variable parameters, without any correlated bias errors.

TABLE III: Pressure measurements (cf. Fig. 1(c)).

Points	1	2	3	4	5	6	7	8	9	
p (kph)	-0.14	-0.16	-0.4	-0.37	-0.18	-0.17	-0.34	-0.32	-0.33	
	10	11	12	13	14	15	16	17	18	av
	-0.31	-0.13	-0.21	-0.3	-0.3	-0.26	-0.27	-0.38	-0.25	-0.6778

TABLE IV: Limits.

Bias limit	Magnitude	Estimation	%-Value
Pressure points	0.01 Kpa	Last significant digit	-3.73%

Then the uncertainty error is calculated

$$U = \sqrt{(-3.73)^2 + (0.31)^2)} \rightarrow U = 3.74\%,$$

confirming that the experimental data accuracy in pressure distribution is more than 96 percent.

III. RESULTS AND DISCUSSION

A. Experiments

In this analysis, we will compare the performance of HDA-1 and HDA-2 against the baseline wing NACA0012 using numerical simulations and experimental data collected from wind tunnel tests. We will begin by examining the aerodynamic characteristics of the various wing designs.

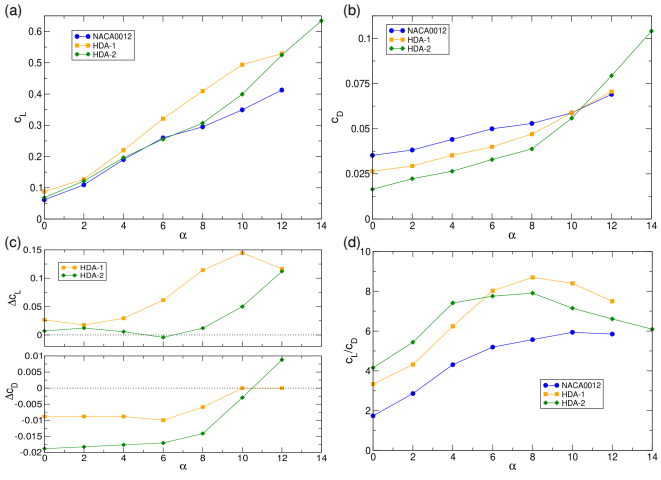

FIG. 5: Experimental results for different wing designs at velocity $v = 22.63m/s$: baseline NACA0012, HDA-1 (1 row of holes) and HDA-2 (2 rows of holes): Variation in AoA for (a) lift coefficient (c_L), (b) drag coefficient (c_D), (c) differences $\Delta c_{L[D]} = c_{L[D]}(\text{HDA-1}) - c_{L[D]}(\text{NACA0012})$ and (d) lift-to-drag ratio c_L/c_D.

Figure 5 illustrates the experimental results for the aerodynamic coefficients, c_L (lift coefficient) and c_D (drag coefficient), as they vary with the angle of attack α for the baseline model NACA0012, HDA-1, and HDA-2 at a selected velocity of $v = 22.63\,m/s$.

For small angles of attack, the lift coefficients c_L for the different wing designs are relatively similar. However, when α exceeds 4 degrees, a notable increase in the slope $c_{L_\alpha(HDA-1)}$ (where $c_L = c_{L_0} + c_{L_\alpha}\alpha$) for HDA-1 is observed compared to the baseline NACA0012 and HDA-2 models (see Fig. $5(a)$). At slightly larger angles, around $\alpha \approx 6$ degrees, the slope $c_{L_\alpha(HDA-2)}$ for HDA-2 also becomes steeper, diverging from the baseline curve in a similar manner. By $\alpha = 12$ degrees, the lift coefficients for HDA-1 and HDA-2 are nearly identical, while they are significantly larger than that of the baseline NACA0012 wing design. Additionally, it is noteworthy that for HDA-2, the stall angle shifts to larger values, approximately $\alpha \approx 15$ degrees.

For angles of attack less than 8 degrees, the drag coefficients c_D increase similarly across all three wing designs. However, the values for HDA-1 and HDA-2 are lower than that of the baseline NACA0012 design (see Fig. $5(b)$), with HDA-2 exhibiting the smallest drag coefficients. A significant change occurs for angles larger than 8 degrees, where the values for HDA-1 and the baseline model converge, while HDA-2 shows a marked increase in drag.

The advantages of HDA-1 and HDA-2 over the baseline NACA0012 design are clearly demonstrated in Fig. $5(c)$, which highlights the differences $\Delta c_{L[D]} = c_{L[D]}(\text{HDA-1}) - c_{L[D]}(\text{NACA0012})$ and $\Delta c_{L[D]} = c_{L[D]}(\text{HDA-2}) - c_{L[D]}(\text{NACA0012})$. In particular, the deviation Δ_{c_L} for HDA-1 is significant over a wide range, specifically between $6° < \alpha < 12°$, peaking around $\alpha \approx 10$ degrees. Meanwhile, the deviations Δ_{c_L} for HDA-2 continue to increase for angles greater than 8 degrees, whereas Δ_{c_D} changes conversely (negatively), indicating an increase in drag.

When comparing the efficiency, measured by the lift-to-drag ratio c_L/c_D (see Fig. $5(d)$), both HDA-1 and HDA-2 exhibit a notable advantage over the baseline NACA0012 wing design, with performance increases of up to 40% depending on angle of attack. The most significant advantage is found in the range of $5° < \alpha < 10°$. Overall, HDA-1 delivers the best efficiency, while HDA-2 achieves the highest lift-to-drag ratio at smaller angles, specifically between $3° < \alpha < 6°$, compared to HDA-1?s optimum range of $6° < \alpha < 10°$. For angles beyond the separation point ($\alpha > 14$), there is a significant rise in drag along with a notable decrease in lift following the separation event.

To gain a deeper understanding of the dynamics, we begin by examining two distinct airfoil profiles: the first row, representing HDA-1, and the second row, representing HDA-2. These profiles intersect with both the large and small holes. Eighteen pressure points, labeled in Fig. $4(b)$, are distributed across the two rows and are connected to a wind tunnel. We analyzed the results and compared them to the corresponding pressure distribution of the baseline model NACA0012.

Figure 6 illustrates the experimental results for the pressure distribution c_p on the upper and lower surfaces of the airfoils, non-dimensionalized by the chord length x/c. The profiles shown are: (a) NACA0012, (b) HDA-1 (1st row of airfoil), and (c) HDA-2 (2nd row of airfoil). The gray areas in (b) and (c) indicate the hole sections.

The figure reveals that the hole down arrays (holes) alter the surface pressure compared to the original

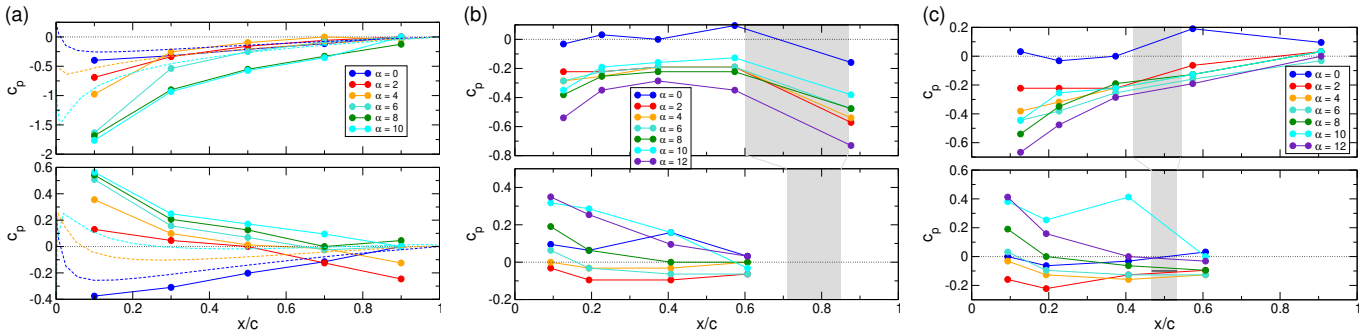

FIG. 6: Experimental results for pressure distribution: (see Fig. 4(b)) (a) NACA0012 profile, (b) HDA-1 (1st row of airfoil), (c) HDA-2 (2nd row of airfoil). Shown are pressure distribution c_p on upper and lower surface (non-dimensionalized by chord length x/c), respectively, for α as indicated. Gray colored areas in (b) and (c) indicate the hole sections. For comparison, the dashed lines in (a) illustrate numerical results of the basic NACA0012 profile (2D simulations) for three different angles $\alpha = 0, 4, 10$ (color code accordingly).

NACA0012 airfoil. According to Bernoulli's theorem, higher flow velocities correspond to lower pressures, implying that the airfoil increases its lift. For NACA0012, the classical behavior with increasing angle of attack α has been confirmed, showing a decrease in c_p on the upper surface while c_p increases on the lower surface. In both cases, the largest variations appear close to the leading edge.

For HDA-1, a qualitatively similar behavior is observed on the lower surface, although with a noticeable offset towards lower values (Fig. 6(b)). On the upper surface, two main differences can be noted. First, the decrease in c_p is much smaller near the leading edge, and a region of almost constant c_p appears over the center of the airfoil, close to the open section/hole. In this plateau region, c_p is significantly smaller (well below $c_p = 0$) than the corresponding values for NACA0012. Second, after the hole, there is a significant drop in c_p, which is completely different from the behavior of c_p for the baseline NACA0012 design. Consequently, the HDA-1 airfoil exhibits a much lower pressure on the upper surface near the trailing edge, and as α increases, the pressure decreases even further. This enhances the pressure difference towards the lower surface, thereby increasing the ratio c_L/c_D (see Fig. 5(d)).

In contrast, the variations in c_p for HDA-2 (Fig. 6(c)) are qualitatively similar to those of the baseline NACA0012 profile. The curves demonstrate the same behavior with increasing α and mainly differ in terms of magnitude. Specifically, the absolute values of c_p on the upper surface for HDA-2 are about half of those for NACA0012, while the lower surface pressures c_p are in a similar range. This lower absolute pressure on the upper surface near the leading edge leads to a variation in the pressure difference, ultimately resulting in a higher lift coefficient, a lower drag coefficient, and improved aerodynamic performance c_L/c_D (see Fig. 5(d)).

Based on the pressure distribution, the HDA-2 profile, with the smaller hole close to the center of the airfoil, has a lesser impact on the overall pressure distribution, while HDA-1 results in significant modifications. However, for both designs, HDA-1 and HDA-2, the experimental results indicate a clear increase in efficiency compared to NACA0012.

In order to confirm the former mentioned observation regarding the flow (direction) inside the holes we tried to visualize the flow in the experiment. Therefore, thin pieces of colored paper have been at the leading edge of each hole's entrance (Fig. 4(d)) on the upper surface in order to observe the flow direction. The paper on the smaller forward hole is sucked into the hole, indicating that the stream direction is from top to bottom, while the colored paper on the big hole (close to trailing edge) is pushed upwards raised, indicating that here the flow direction is just opposite, from bottom to top.

B. Simulations

1. *2D simulations*

Due to the high costs and limitations of large-scale three-dimensional simulations, we conducted 2D numerical simulations of the various airfoil profiles featured in HDA-1 and HDA-2. The results are presented in Fig. 7, reflecting the format of the experimental data shown in Fig. 5. As expected, the basic NACA0012 airfoil demonstrated the best performance in the 2D simulations, exhibiting the highest lift and the best aerodynamic efficiency, as indicated by the lift-to-drag ratio.

These results align with our expectations, since the presence of different holes in 2D can significantly disrupt airflow. The advantages of the HDA-1 and HDA-2 designs become evident only in 3D simulations. In that case, a three-dimensional flow can be observed within the holes, interacting with the flow on the extrados and intrados, which positively influences the overall dynamics.

This result clearly shows the importance of a third di-

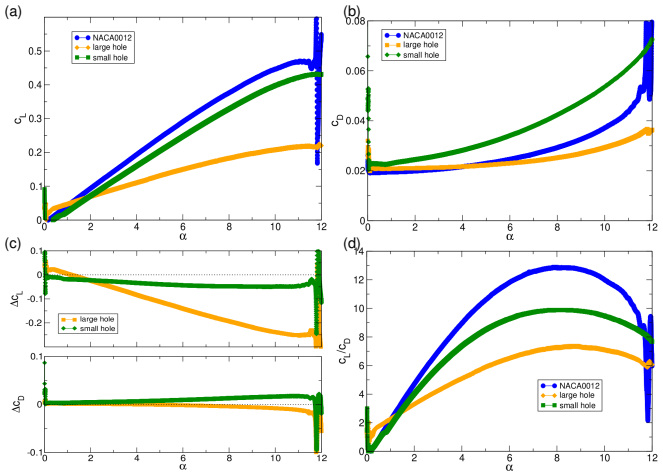

FIG. 7: 2D numerical results for different wing designs at velocity $v = 22.63m/s$: baseline NACA0012, airfoil with large hole and airfoil with small hole: Variation in AoA for (a) lift coefficient (c_L), (b) drag coefficient (c_D), (c) differences $\Delta c_{L[D]} = c_{L[D]}(\text{A,B}) - c_{L[D]}(\text{NACA0012})$ and (d) lift-to-drag ratio c_L/c_D (cf. Fig. 5)

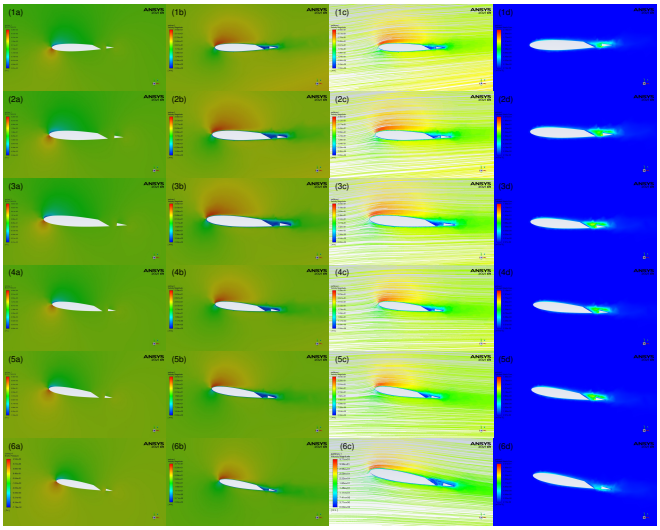

FIG. 8: 2D Flow visualizations inside the hole that is closest to the trailing edge (HDA-1 design, cf. Fig. 2, 1st row) for different angle of attack (1) $\alpha = 0$, (2) $\alpha = 2$, (3) $\alpha = 4$, (4) $\alpha = 6$, (5) $\alpha = 8$, and (6) $\alpha = 10$. Shown are (a) the static pressure, (b), the stream velocity and (c) flow lines ($v = 22.63m/s$), and (d) the turbulent kinetic energy.

mension and highlights the limitations of basic 2D simulations. For a realistic representation, the entire wing must be simulated.

a. Large hole In the following, we will closely examine the 2D dynamics related to the open sections of HDA-1 and HDA-2 airfoils, specifically how these modifications impact flow separation over the airfoil with variations in angle of attack (α) ranging from 0° to 14°.

Figure 8 illustrates the evolution of several key characteristics as α changes for HDA-1. The figure includes contour plots of (a) static pressure, (b) stream velocity, (c) flow line visualizations, and (d) turbulent kinetic energy. As expected, the high stagnation pressure zone (shown in Fig. 8(a)) shifts along the curvature of the lower leading edge of the airfoil as α increases. This movement is unaffected by the hole, as its position is located further back on the airfoil.

The velocity magnitude and streamlines (Fig. 8(b, c)) exhibit a similar pattern; the zero-velocity stagnation point moves along the lower surface of the airfoil while the airflow accelerates along the leading edge on the upper surface as α increases. The contour plots of turbulent intensity (Fig. 8(d)) present an intriguing observation: as α increases (noting that turbulent intensity levels vary slightly across each plot), the plots reveal a smaller region of higher turbulent intensity, particularly at the largest angle of attack, $\alpha = 10°$. Notably, this area is also positioned closer to the intradus. It is important to mention that separation occurs at approximately $\alpha = 12°$.

b. Small hole Similar to the analysis of HDA-1 (Fig. 8), Fig. 9 illustrates the evolution of various characteristic quantities as the angle of attack, α, changes for HDA-2. The contour plots of (a) the static pressure remain largely unaffected by the hole, with the high stagnation pressure zone (Fig. 9(a)) shifting along the curvature of the lower leading edge of the airfoil as α increases. However, there is a slight modification in the velocities. As α increases, the zero-velocity stagnation point shifts along the lower surface of the airfoil, while the air accelerates along the leading edge on the upper surface. The opening of the hole on the extrados acts as a limiting point.

Both the magnitude of velocity and streamlines (Fig. 8(b, c)) emphasize this behavior. Meanwhile, as expected, the turbulent intensity contour plots (Fig. 9(d)) reveal a broader zone of higher turbulent intensity with increasing α, which is caused by the central position of the hole.

Figure 10 illustrates the effects of different hole configurations on flow dynamics at an angle of attack (α) of 16 degrees, which is beyond the stall angle (approximately $\alpha \approx 12$ degrees). In all cases, the flow is largely fully separated from the leading edge. In the case of NACA0012 (Fig. 10(a)), there is a well-known scenario in which one large vortex forms above the airfoil in the extradus, accompanied by a smaller but stronger vortex located behind the airfoil. The trailing edge serves as the boundary separating these two vortices. The interaction between them results in alternating, wavy-like flow dynamics observed behind the airfoil. For both airfoils featuring holes, a third vortex appears above the holes in the extradus. This occurs due to potential pressure exchange between the extradus and intradus through the holes, leading to significant modifications compared to the basic NACA0012 profile. In addition to the obvious third vortex structure, the vortex situated behind the airfoil in NACA0012 (Fig. 10(a)) shifts forward onto

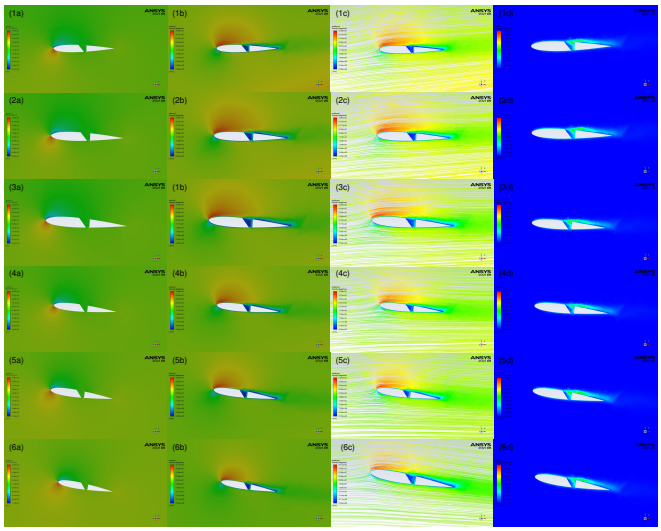

FIG. 9: 2D Flow visualizations inside the hole that is closest to the leading edge (HDA-2 design, cf. Fig. 2, 2nd row) for different angle of attack (1) $\alpha = 0$, (2) $\alpha = 2$, (3) $\alpha = 4$, (4) $\alpha = 6$, (5) $\alpha = 8$, and (6) $\alpha = 10$. Shown are (a) the static pressure, (b), the stream velocity and (c) flow lines ($v = 22.63m/s$) and (c) flow lines ($v = 22.63m/s$), and (d) the turbulent kinetic energy.

the extradus. This shift is relatively moderate for the large hole (Fig. 10(b)), but in the case of the small hole, this vortex moves completely on top of the extradus (Fig. 10(c)).

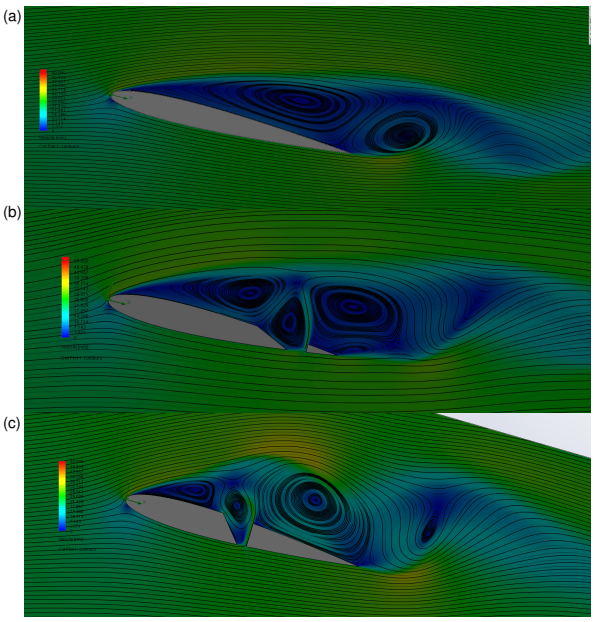

FIG. 10: Comparison of the 2D flow dynamics beyond stall $\alpha = 16$ for different airfoil profiles. (a) basic NACA0012, and (b) large hole (see Fig. 8), and (c) small hole (see Fig. 9). Shown is the streamwise velocity ($v = 22.63m/s$).

2. 3D simulations

To gain a better understanding of the necessity for three-dimensionality and to validate our experimental results, we performed full 3D simulations for HDA-2 at selected parameters. These simulations provide a clear illustration of the evolving flow dynamics.

Figure 11 displays the streamlines for HDA-2 from different perspectives: (a) a view from the leading edge, (b) a close-up view, (c) a top view and (d) a bottom view. It is evident that the upper surface is significantly more affected than the lower surface due to the hole openings. Vortices begin to form on the upper side of the wings around these openings and continue to evolve over the wing, extending beyond the trailing edge.

To understand the effects and dynamics within the holes, Fig. 12 presents various close-ups of the hole sections, viewed from the intradus (lower surface) and extradus (upper surface). As observed in the general view (Fig. 11), the velocity streamlines on the lower surface (intradus) are only minimally affected. For both the large hole configuration (Fig. 12$(a1)$) and the small hole configuration (Fig. 12$(b1)$), most streamlines continue unaffected over the opening, with only a few entering the cap and generating internal upstream flow.

Interestingly, in the case of the small front hole (Fig. 12$(b1)$), the flow enters smoothly in a straight forward direction. In contrast, the large hole configuration (Fig. 12$(a1)$) immediately develops a vortex structure. This vortex evolves into two counterrotating vortices toward the extradus in the large hole (Fig. 12$(a2)$), significantly affecting the overall flow dynamics as it exits the gap, as seen in the broader view (Fig. 11(a)).

Within the small hole configuration (Fig. 12$(b1)$), a vortex structure also forms as it moves towards the extradus. However, in this case, there is primarily a single vortex, which interferes with the streamlines on the extradus, but to a significantly lesser extent, resulting in 'smoother' streamlines over the extradus (Fig. 12$(b2)$). This vortex appears to be more 'stuck' or held within the hole.

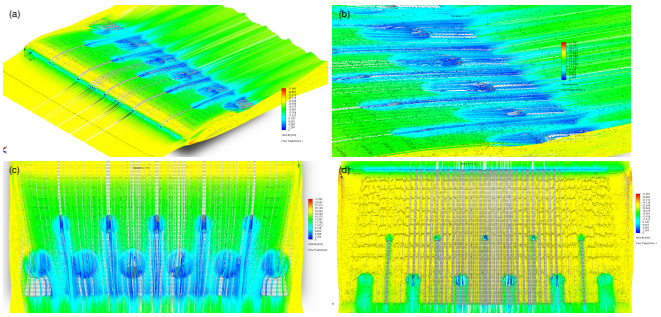

FIG. 11: Flow visualization of the velocity field for HDA-2 at $\alpha = 0$ and $v = 22.63m/s$ around the wing. Views from (a) the leading edge with (b) being a close up and further view from the top (c) and bottom (d), respectively.

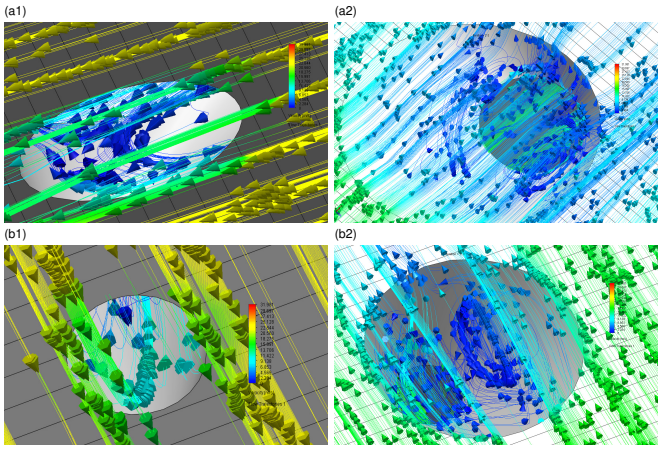

FIG. 12: Flow visualization for $\alpha = 0$ and $v = 22.63m/s$ of the dynamics within the holes. (a) Bottom view of the flow over a section including two big (back) and one small (front) canonical hole. Close-up of the insight evolving flow for (a) the back big hole seen from the (1) intradus and (2) extradus, respectively, and (b) the front small hole seen from the (1) intradus and (2) extradus, respectively.

IV. CONCLUSION

This article investigates the possibilities of passive flow control through a novel hole-down-array (HDA) wing design. Two different HDAs were tested: one with a single row of holes (HDA-1) and another with two staggered rows of holes (HDA-2). The holes were positioned either in the center of the airfoil or toward the trailing edge. For comparison, a classical airfoil design, referred to as NACA0012, was used as a baseline.

Both numerical simulations and experimental wind tunnel tests were conducted to analyze the aerodynamic performance and efficiency of the new designs. Numerous parametric studies were carried out to critically examine the influence of various parameters. In particular, the dependence of the aerodynamic coefficients c_L, c_D, and c_p on the angle of attack α was analyzed.

In general, it was found that the new designs significantly affect the flow on the extrados of the wing, while the flow on the intrados is only minimally modified. This aligns with the general observation of upward-directed flow within the holes. Our findings indicate that the new designs have improved the aerodynamic characteristics, resulting in higher efficiency.

Based on our findings regarding the different flow strengths and directions within the holes in HDA-1 and HDA-2, our next goal is to control the direction of airflow within these holes. Modifying this airflow can influence flying conditions and potentially improve efficiency. However, how this can be achieved remains an open question and is beyond the scope of the current study; it will be addressed in future investigations.

One possibility is to implement a door system that can open and close the arrays. Therefore, our future work will explore the installation of control valves on one or both sides of the holes. This would allow us to manage airflow and adjust the system to meet more specific parameter settings.

Furthermore, our results clearly demonstrate the necessity of considering the third dimension and highlight the limitations of relying solely on 'simple' 2D simulations. While 2D simulations may be useful for basic geometries, a comprehensive and realistic understanding requires simulating the full wing.

Acknowledgments

S. A. is a Serra Húnter Fellow. This work is supported by the Spanish Government under grants PID2023-150014OB-C21 and PID2023-150029NB-I00

Data Availability Statement

The data that support the findings of this study are available from the corresponding author upon reasonable request.

Conflicts of Interest

The authors declare no conflicts of interest.

[1] D. Lasagna, R. Donelli, F. D. Gregori, and G. Iuso, Experiments in Fluids **51**, 1369 (2011).
[2] C. Panigrahi, R. Chawla, and M. T. Nair, Journal of Applied Fluid Mechanics **15**, 179 (2022).
[3] F. O. Ringleb, 48th AIAA Aerospace Sciences Meeting **1**, 265 (1961).
[4] R. Adkins, Journal of Fluids Engineering **97**, 297 (1975).
[5] C. Rowley, V. Juttijudata, and D. Williams, 43rd AIAA Aerospace Sciences Meeting and Exhibit p. 292 (2005).
[6] A. Iollo and L. Zannetti, European Journal of MechanicsB/Fluids **20**, 7 (2001).
[7] M. Rahman, M. A. Hossain, M. N. Uddin, and M. Mashud, Proceedings of the International Conference on Mechanical Engineering and Renewable Energy (2015).
[8] H. Shan, L. Jiang, C. Liu, M. Love, and B. Maines, Computers and Fluids **37**, 975 (2008).
[9] K. N. Abed, Diyala Journal of Engineering Sciences **12**, 99 (2019).
[10] L. Hao, Y. Gao, and B. Wei, International Journal of

Aeronautical and Space Sciences (2022) 23: **23**, 859 (2022).
[11] I. H. Ibrahim, J. Joy, and T. N. New, 46th AIAA Fluid Dynamics Conference (2016).
[12] W. L. Siauw, J.-P. Bonnet, J. Tensi, L. Cordier, B. R. Noack, and L. Cattafesta, International Journal of Heat and Fluid Flow **31**, 450 (2010).
[13] R. Raju and R. Mittal, AIAA JOURNAL 46, No. 12, December 2008 **46** (2008).
[14] D. You and P. Moin, Center for Turbulence Research - Annual Research Briefs (2007).
[15] L. N. Cattafesta and M. Sheplak, Annual Review of Fluid Mechanics **43**, 247 (2011).
[16] F. Sonkaya, S. Cadirci, and D. Erdem, Journal of Applied Fluid Mechanics **15**, 427 (2022).
[17] A. Seifert, T. Bachar, D. Koss, M. Shepshelovich, and I. Wygnanski, AIAA Journal **31**, 2052 (1993).
[18] G. Godard, J. M. Foucaut, and M. Stanislas, Aerospace Science and Technology **10**, 394 (2006).
[19] Q. Dai, E. Qi, S. Huang, Z. Zhou, and Y. Wang, Journal of Applied Fluid Mechanics **17**, 1293 (2024).
[20] Y. Xie, J. Chen, H. Qu, G. Xie, D. Zhang, , and M. Moshfeghi, Hindawi Publishing Corporation Mathematical Problems in Engineering p. 14 (2013).
[21] A. R. Paul, A. Mittal, and A. Jain, Proceedings of the Thirty Ninth National Conference on Fluid Mechanics and Fluid Power **228** (2012).
[22] R. Lockwood, J. P. Swaddle, and J. M. V. Rayner, Journal of Avian Biology **29**, 273 (1998).
[23] W. Shyy, M. Berg, and D. Ljungqvist, Progress in Aerospace Science **35**, 455 (1999).
[24] T. J. Feo, D. J. Field, and R. O. Prum, Proceedings of the Royal Society B: Biological Sciences **282**, 20142864 (2015).
[25] D. Liu, B. Song, W. Yang, X. Yang, D. Xue, and X. Lang, Journal of Bionic Engineering **18**, 1255 (2021).
[26] T. Grager, A. Rothmayer, and H. Hu, 49th AIAA Aerospace Sciences Meeting including the New Horizons Forum and Aerospace Exposition, Florida, USA pp. 1–10 (2011).